Brillouin-zone unfolding of perfect supercells having nonequivalent primitive cells illustrated with a Si/Ge tight-binding parameterization

Timothy B. Boykin
Department of Electrical and Computer Engineering, The University of Alabama in Huntsville, Huntsville, Alabama 35899, USA

Neerav Kharche and Gerhard Klimeck
Network for Computational Nanotechnology, School of Electrical and Computer Engineering, Purdue University, West Lafayette, Indiana 47907, USA

(Received 20 March 2007; published 11 July 2007)

Numerical calculations of nanostructure electronic properties are often based on a nonprimitive rectangular unit cell, because the rectangular geometry allows for both highly efficient algorithms and ease of debugging while having no drawback in calculating quantum dot energy levels or the one-dimensional energy bands of nanowires. Since general nanostructure programs can also handle superlattices, it is natural to apply them to these structures as well, but here problems arise due to the fact that the rectangular unit cell is generally not the primitive cell of the superlattice, so that the resulting $E(\mathbf{k})$ relations must be unfolded to obtain the primitive-cell $E(\mathbf{k})$ curves. If all of the primitive cells in the rectangular unit cell are identical, then the unfolding is reasonably straightforward; if not, the problem becomes more difficult. Here, we provide a method for zone unfolding when the primitive cells in a rectangular cell are not all identical. The method is applied to a Si(4)Ge(4) superlattice using a set of optimized Si and Ge tight-binding strain parameters.

DOI: 10.1103/PhysRevB.76.035310 PACS number(s): 73.21.Cd, 71.15.−m, 73.61.Cw

I. INTRODUCTION

Most semiconductor nanostructures are made from materials which adopt a rectangular geometry of some sort. For example, fcc is the lattice for the most common semiconductors: Si (diamond) and GaAs (zinc blende). In addition, many technologically important nanostrucutures such as superlattices (SLs), resonant-tunneling diodes, ultrascaled metal-oxide-semiconductor field-effect transistors, quantum wells, and nanowires are constructed as layers, so that the rectangular geometry persists, even in the presence of strain. Embedded objects such as self-assembled quantum dots are also easily modeled with rectangular unit cells of differing composition. Due to the rectangular geometry, grouping atoms into eight-atom zinc-blende-like conventional unit cells yields a simplified treatment and storage scheme for relative atom coordination. The result is generally more efficient and easily debugged algorithms, making the choice attractive from a computational perspective as well. A rectangular cell—even a nonprimitive one—is therefore a natural choice for the underlying building block of a general nanodevice modeling tool such as NEMO3D.[1,2]

Although using a nonprimitive rectangular unit cell to calculate $E(\mathbf{k})$ relations for superlattices or bulk semiconductors simplifies the boundary conditions, the results can be difficult to relate back to the primitive-cell $E(\mathbf{k})$ relations due to zone folding. The zone-unfolding process is more complicated if the true primitive cell is not rectangular. For bulk semiconductors such as Si or GaAs, the conventional fcc unit cube contains four identical primitive cells (rhombahedra), and the periodic boundary conditions are applied over the cube instead of over N_i primitive cells along each of the (nonorthogonal) primitive cell vectors $\mathbf{a}_i$. For this case, our zone-unfolding method[3] can be used in its original formulation, but with a different choice of allowed wave vectors.[4,5]

A more difficult complication arising from the use of a nonprimitive rectangular cell can occur in modeling superlattices. A specific example is the Si(4)Ge(4) SL fabricated and studied experimentally by Pearsall *et al.*[6] and theoretically using the linear muffin-tin orbital (LMTO) method by Ikeda *et al.*[7] Each primitive cell of this SL has eight atoms, so a natural choice for a nonprimitive rectangular cell is a stack of two eight-atom rectangular cells. Were strain absent, each eight-atom rectangular cell would simply be a conventional fcc cube. This rectangular cell is by far the easiest to implement, since its faces are perpendicular to the Cartesian axes. Moreover, it is compatible with many common nanodevice geometries.

Unfortunately, it is not compatible with this SL, since two identical SL primitive cells do not fit into this "conventional" nonprimitive cell as shown in Fig. 1. The filled atoms (striped for Si, dotted for Ge) belong to the two primitive SL unit cells (transparent rectangular boxes). Open atoms belong to other SL primitive cells and are shown to delineate the boundaries of the nonprimitive rectangular cell. The atoms of cell 0 (forward SL primitive cell) are labeled $j=0,\ldots,7$; the atoms of cell 1 (rearward SL primitive cell) are not labeled. Observe that atoms 3 and 7 of SL primitive cell 1 actually lie outside the rear face of the nonprimitive rectangular cell. Thus, two identical primitive cells of this SL do not fit into a conventional, rectangular nonprimitive cell.

If one allows the two SL primitive cells to differ, then both can be contained in the conventional rectangular cell, as shown in Fig. 2. This nonprimitive rectangular cell also contains 16 atoms, with indices as (n,j), $n=0,1$, $j=0,\ldots,7$, where n is the SL primitive-cell index and j the index of the atom within the cell. Note that the two SL primitive cells of Fig. 2 are different. Cell 0 is identical to the forward primitive cell of Fig. 1 (cell with numbered atoms). Cell 1 has atoms 2, 3, 6, and 7 translated $a_{\|}\mathbf{e}_x$ relative to their counter-

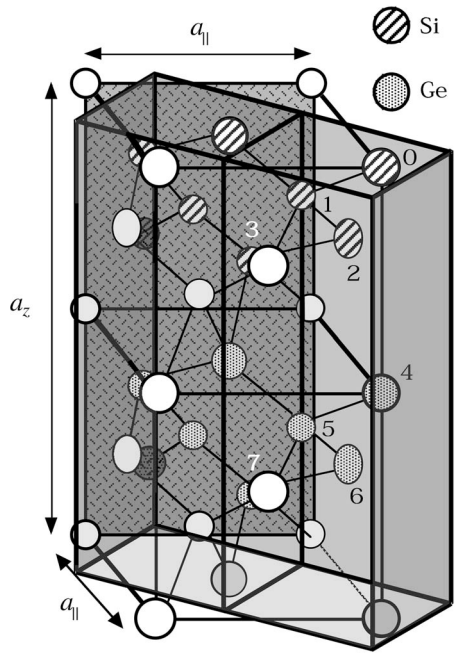

FIG. 1. Two identical primitive cells of the Si(4)Ge(4) SL studied here and in Refs. 6 and 7. Atoms included in the two primitive cells are shaded (Si, stripes; Ge, dots); atoms belonging to other primitive cells are open and are shown to clearly delineate a rectangular, nonprimitive cell used to locate the origin of the two-primitive-cell pair. The rear wall of the rectangular cell is shaded, and atoms 3 and 7 of the rearward primitive cell lie behind it.

parts in the rearward primitive cell of Fig. 1. Repeating the nonprimitive rectangular cell of Fig. 2 throughout all space generates the SL, so it should be possible to extract the small-cell bands from an electronic structure calculation based on it. However, because these two primitive cells are not equivalent, the method for zone unfolding is not immediately obvious.

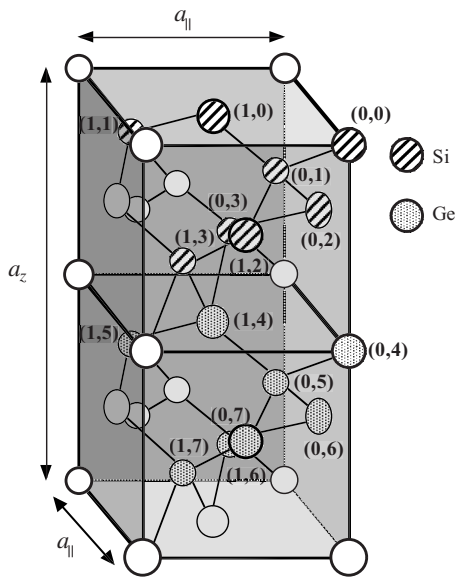

FIG. 2. Rectangular, nonprimitive cell used here in band structure calculations for the Si(4)Ge(4) SL; the atoms are indexed as (primitive cell, atom). The two primitive cells are not identical, as is clear from the differing relative positions of atoms 2, 3, 6, and 7.

The dilemma posed by the rectangular cell of Fig. 2 needs resolution, since it is impractical to change the primitive-cell definition in a general nanostructure modeling tool. For the case of the SL discussed above, one solution would be to use a nonprimitive (and nonconventional) rectangular cell with x and y axes rotated by 45°. However, doing so in a calculation based on conventional rectangular cells would require major alterations to the critical supercell electronic structure algorithm. If one must make such changes for each SL geometry, then the tool is hardly general. Because any rectangular unit cell chosen might well be suitable for some SLs but not for others, a better resolution is to find a method by which the primitive-cell bands may be recovered even with a unit cell like that in Fig. 2, where the primitive cells are different. This solution preserves the generality of the tool, since the underlying rectangular cell need not be changed and the SL-specific algorithmic modifications come *after* the electronic structure calculation.

In this work, we modify our Brillouin-zone-unfolding method[3–5] so that it can recover the primitive cell $E(\mathbf{k})$ relations from a nonprimitive rectangular cell such as that in Fig. 2. We illustrate the method for the Si(4)Ge(4) SL studied in Refs. 6 and 7 using the $sp^3d^5s^*$ empirical tight-binding model[8] with our room-temperature bulk Si and Ge parameters.[9] Because strain is present in the SL, we provide here a set of strain parameters for Si and Ge which incorporates diagonal parameter shifts due to nearest-neighbor interactions. We find good agreement with the results of Refs. 6 and 7.

II. METHOD

A. Allowed wave vectors

The first step in recovering the primitive cell $E(\mathbf{k})$ relations from those of the nonprimitive cell is the determination of the allowed primitive-cell wave vectors and their relationship to the nonprimitive-cell wave vectors. As shown in Fig. 2, the nonprimitive rectangular cell has direct lattice vectors

$$\mathbf{A}_1 = a_\parallel \mathbf{e}_x, \quad \mathbf{A}_2 = a_\parallel \mathbf{e}_y, \quad \mathbf{A}_3 = a_z \mathbf{e}_z, \tag{1}$$

whereas the primitive cell of Fig. 1 has direct lattice vectors

$$\mathbf{a}_1 = \frac{a_\parallel}{2}(\mathbf{e}_x + \mathbf{e}_y), \quad \mathbf{a}_2 = \frac{a_\parallel}{2}(\mathbf{e}_x - \mathbf{e}_y), \quad \mathbf{a}_3 = a_z \mathbf{e}_z. \tag{2}$$

Thus, the nonprimitive cell is exactly twice the volume of the primitive cell. The primitive-cell reciprocal lattice vectors are therefore

$$\mathbf{b}_1 = \frac{2\pi}{a_\parallel}(\mathbf{e}_x + \mathbf{e}_y), \quad \mathbf{b}_2 = \frac{2\pi}{a_\parallel}(\mathbf{e}_x - \mathbf{e}_y), \quad \mathbf{b}_3 = \frac{2\pi}{a_z}\mathbf{e}_z. \tag{3}$$

The primitive-cell Brillouin zone is thus a rectangular parallelepiped, rotated so that its projection in the x-y plane is a diamond (Fig. 3). The Brillouin zone of the nonprimitive rectangular cell is also a rectangular parallelepiped, with sides perpendicular to the Cartesian axes. Figure 3 shows the

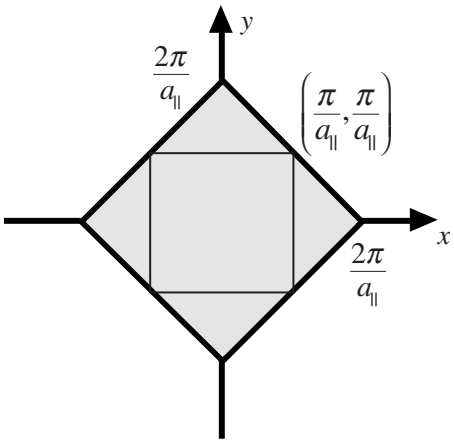

FIG. 3. Cross sections in the x-y plane of the Brillouin zones of the true primitive cell (large diamond) and the rectangular, nonprimitive cell (small inscribed square) for the Si(4)Ge(4)SL.

projections of these zones in the plane, the diamond being that of the primitive cell and the smaller inscribed square being that of the nonprimitive rectangular cell. Both zones have the same z length: $-\pi/a_z < k_z \leqslant \pi/a_z$.

The allowed wave vectors are determined by enforcing periodic boundary conditions on the wave function over an integral number of nonprimitive cells in each of the directions $\mathbf{A}_i$, $i=1,2,3$:

$$\psi(\mathbf{r}+N_i\mathbf{A}_i)=\psi(\mathbf{r}), \quad i=1,2,3. \tag{4}$$

These boundary conditions yield the familiar set of allowed supercell wave vectors $\mathbf{K}_\mathbf{n}$, $\mathbf{n}=(n_1,n_2,n_3)$:

$$\mathbf{K}_\mathbf{n}=2\pi\left[\frac{n_1}{N_1a_\parallel}\mathbf{e}_x+\frac{n_2}{N_2a_\parallel}\mathbf{e}_y+\frac{n_3}{N_za_z}\mathbf{e}_z\right], \tag{5}$$

$$n_i=\begin{cases}-\dfrac{N_i-2}{2},\ldots,\dfrac{N_i}{2}, & N_i \text{ even}\\ -\dfrac{N_i-1}{2},\ldots,\dfrac{N_i-1}{2}, & N_i \text{ odd}.\end{cases} \tag{6}$$

For each of the $N_1\times N_2\times N_3$ supercell wave vectors $\mathbf{K}_\mathbf{n}$, there must be *two* primitive cell wave vectors since each nonprimitive cell contains two primitive cells. One primitive-cell wave vector is obviously just $\mathbf{K}_\mathbf{n}$, since the nonprimitive-cell Brillouin zone is entirely contained within the primitive-cell Brillouin zone (Fig. 3). The other primitive-cell wave vector is found by applying periodic boundary conditions over a single nonprimitive cell, i.e., $N_1=N_2=N_3=1$ in Eq. (4). For the single nonprimitive cell, the only supercell wave vector is therefore $\mathbf{K}_\mathbf{n}=\mathbf{0}$, which is likewise one of the two allowed primitive-cell wave vectors. The other is the supercell reciprocal lattice vector $\mathbf{G}=(2\pi/a_\parallel)\mathbf{e}_x$, lying at the vertex of the primitive-cell Brillouin zone (Fig. 3), which satisfies periodic boundary conditions over the nonprimitive cell. This conclusion follows from writing the wave function in Bloch form:

$$\psi_\mathbf{k}(\mathbf{r})=e^{i\mathbf{k}\cdot\mathbf{r}}u_\mathbf{k}(\mathbf{r}), \quad u_\mathbf{k}(\mathbf{r}+N_i\mathbf{A}_i)=u_\mathbf{k}(\mathbf{r}), \quad i=1,2,3 \tag{7}$$

$$\begin{aligned}\Rightarrow\psi_\mathbf{G}(\mathbf{r}+a_\parallel\mathbf{e}_x)&=e^{i(2\pi/a_\parallel)(x+a_\parallel)}u_\mathbf{G}(\mathbf{r}+a_\parallel\mathbf{e}_x)\\&=e^{i(2\pi/a_\parallel)x}u_\mathbf{G}(\mathbf{r})=\psi_\mathbf{G}(\mathbf{r}).\end{aligned} \tag{8}$$

Because $\mathbf{G}=(2\pi/a_\parallel)\mathbf{e}_x$ obviously satisfies periodic boundary conditions over any integral number of nonprimitive cells in each of the directions $\mathbf{A}_i$, it follows that the allowed primitive-cell wave vectors are thus

$$\mathbf{k}_{\mathbf{n},j}=\mathbf{K}_\mathbf{n}+\mathbf{G}_j, \quad j=0,1, \quad \mathbf{G}_0=0, \quad \mathbf{G}_1=\frac{2\pi}{a_\parallel}\mathbf{e}_x. \tag{9}$$

Note that it may be necessary to shift the $\mathbf{k}_{\mathbf{n},j}$ back into the primitive-cell first Brillouin zone, but this is easily accomplished (see Ref. 4). Also, observe that $(2\pi/a_\parallel)\mathbf{e}_y$ is not independent since it differs from $\mathbf{G}_1$ by a primitive-cell reciprocal lattice vector: $(2\pi/a_\parallel)\mathbf{e}_y=\mathbf{G}_1-\mathbf{b}_2$.

B. Modified projection method

Extracting the primitive-cell $E(\mathbf{k})$ relations from those of the nonprimitive cell involves relating the wave functions in the nonprimitive rectangular cell basis and the primitive-cell basis. Because the two primitive cells in the rectangular cell of Fig. 2 are not identical, we adopt a slightly different notation from that employed in Refs. 3 and 5. An atomiclike orbital in the σ basis (p for primitive, s for supercell or nonprimitive) is written as $|\alpha;\mathbf{X}^\sigma_{\mathbf{m},l,j}\rangle$, where α is a composite index encompassing the orbital type (s, p_x, etc.), spin, and species, and $\mathbf{X}^\sigma_{\mathbf{m},l,j}$ gives the atom location. The integer trio $\mathbf{m}=(m_1,m_2,m_3)$ indexes a 16-atom rectangular cell, l indexes one of its two eight-atom primitive cells, and j indexes one of the eight atoms.

In the primitive-cell basis, the locations are specified as

$$\mathbf{X}^p_{\mathbf{m},l,j}=\mathbf{R}_\mathbf{m}+\boldsymbol{\rho}_l+\boldsymbol{\delta}_j, \tag{10}$$

$$\mathbf{R}_\mathbf{m}=\sum_{i=1}^{3}m_i\mathbf{A}_i, \quad \boldsymbol{\rho}_0=\mathbf{0}, \quad \boldsymbol{\rho}_1=-\mathbf{a}_1, \tag{11}$$

where the nonprimitive and primitive direct lattice vectors are given in Eqs. (1) and (2). The exact specification of the $\boldsymbol{\delta}_j$ is not critical for deriving the method. Recall from the introduction that atoms 3 and 7 of primitive cell 1 for a given 16-atom rectangular cell $\mathbf{m}$ actually lie outside the rear wall of the cell. This poses no difficulty, though, since we only use the rectangular cell to locate the origin (atom 0, primitive cell 0) of a pair of two identical primitive cells.

In the nonprimitive or supercell basis, the atom locations (see Fig. 2) are specified as

$$\mathbf{X}^s_{\mathbf{m},l,j}=\mathbf{R}_\mathbf{m}+\boldsymbol{\rho}_l+\mathbf{d}^{(l)}_j, \tag{12}$$

where $\mathbf{R}_\mathbf{m}$ and $\boldsymbol{\rho}_l$ are defined in Eq. (11) above and

$$\mathbf{d}^{(l)}_j=\boldsymbol{\delta}_j+a_\parallel\mathbf{e}_x\Delta^{(l)}_j, \quad \Delta^{(l)}_j=\begin{cases}0, & l=0;l=1,j=0,1,4,5\\ 1, & l=1,j=2,3,6,7.\end{cases} \tag{13}$$

Comparison of Eq. (10) and Eqs. (12) and (13) reveals that

$$\mathbf{X}^s_{\mathbf{m},l,j}=\mathbf{X}^p_{\mathbf{m},l,j}, \quad l=0; \quad l=1, \quad j=0,1,4,5, \tag{14}$$

$$\mathbf{X}^{s}_{\mathbf{m},l,j} = \mathbf{X}^{p}_{\mathbf{m},l,j} + a_{\|}\mathbf{e}_x = \mathbf{X}^{p}_{(m_1+1,m_2,m_3),l,j}, \quad l=1, \quad j=2,3,6,7. \tag{15}$$

Equation (15) shows that on projection of the supercell state onto the primitive-cell basis, atoms 2, 3, 6, and 7 of primitive cell 1 will receive an extra phase factor $\exp(iK_x a_{\|})$.

Projecting the primitive-cell states out of the supercell states proceeds as in Refs. 3 and 5 but subject to the modifications of Eqs. (10)–(15) above. The treatment here is specific to the nonprimitive rectangular cell of Fig. 2. For a SL composed of N_S nonprimitive rectangular cells, the supercell state of energy E_p is written as

$$|\Psi_p(\mathbf{K})\rangle = \sum_{\mathbf{m}}^{\langle N_S\rangle} \sum_{\alpha}^{N_{O,atom}} \sum_{l=0}^{1} \sum_{j=0}^{7} \frac{e^{i\mathbf{K}\cdot\mathbf{R}_\mathbf{m}}}{\sqrt{N_S}} \beta^{(\alpha,j)}_{l,p}(\mathbf{K}) |\alpha; X^{s}_{\mathbf{m},l,j}\rangle, \tag{16}$$

where there are $N_{O,atom}$ orbitals per atom and the notation $\langle N_s\rangle$ on the sum over $\mathbf{m}$ denotes the N_S trios $\mathbf{m}$ which index all rectangular cells of the SL. Cyclic boundary conditions are applied over the N_S rectangular cells.

The supercell states are projected onto the Bloch basis of (identical) primitive cells (Fig. 1 shows two such identical cells). The Bloch basis state of energy E_η and wave vector $\mathbf{k}=\mathbf{K}+\mathbf{G}_n$, $n=0,1$, is therefore written as

$$|\psi_\eta(\mathbf{K}+\mathbf{G}_n)\rangle = \sum_{\mathbf{m}}^{\langle N_S\rangle} \sum_{\alpha}^{N_{O,atom}} \sum_{l=0}^{1} \sum_{j=0}^{7} \frac{e^{i\mathbf{K}\cdot\mathbf{R}_\mathbf{m}}}{\sqrt{2N_S}} b^{(\alpha,j)}_{\eta}(\mathbf{K} + \mathbf{G}_n) e^{i(\mathbf{K}+\mathbf{G}_n)\cdot\boldsymbol{\rho}_l} |\alpha; \mathbf{X}^{p}_{\mathbf{m},l,j}\rangle. \tag{17}$$

The factor of 2 in the square root occurs since there are two primitive cells per rectangular cell (see Fig. 1). The two allowed values of $\mathbf{G}_n$ (there are two primitive cells per supercell) are given in Eq. (9).

At each supercell wave vector $\mathbf{K}$, there are $16N_{O,atom}$ supercell energy bands, while for a primitive cell, there are $8N_{O,atom}$ bands at each $\mathbf{k}=\mathbf{K}+\mathbf{G}_n$, $n=0,1$. Each supercell state is thus a linear combination of all of the primitive-cell states:

$$|\Psi_p(\mathbf{K})\rangle = \sum_{\eta=1}^{8N_{O,atom}} \sum_{n=0}^{1} a_{p;\eta,n} |\psi_\eta(\mathbf{K}+\mathbf{G}_n)\rangle. \tag{18}$$

Taking the inner product of Eq. (18) with $\langle\alpha; \mathbf{X}^{s}_{\mathbf{m},l,j}|$ and employing Eqs. (14) and (15) result in a pair of equations for each atom-orbital pair (α,j), $\alpha=1,\ldots,N_{O,atom}$, $j=0,\ldots,7$:

$$\exp[-i(\mathbf{K}\cdot\boldsymbol{\rho}_l + K_x a_{\|}\Delta^{(j)}_l)]\beta^{(\alpha,j)}_{l,p}(\mathbf{K}) = \frac{1}{\sqrt{2}} \sum_{\eta=1}^{8N_{O,atom}} \sum_{n=0}^{1} e^{i\mathbf{G}_n\cdot\boldsymbol{\rho}_l} a_{p;\eta,n} b^{(\alpha,j)}_{\eta}(\mathbf{K}+\mathbf{G}_n). \tag{19}$$

In matrix form, these equations read

$$\mathbf{B}^{(\alpha,j)}_{p}(\mathbf{K}) = \underline{\mathbf{U}} \cdot \mathbf{C}^{(\alpha,j)}_{p}(\mathbf{K}), \tag{20}$$

where

$$\mathbf{B}^{(\alpha,j)}_{p}(\mathbf{K}) = \begin{bmatrix} e^{-i\mathbf{K}\cdot\boldsymbol{\rho}_0}\beta^{(\alpha,j)}_{0,p}(\mathbf{K}) \\ e^{-i[\mathbf{K}\cdot\boldsymbol{\rho}_1 + K_x a_{\|}\Delta^{(l)}_j]}\beta^{(\alpha,j)}_{1,p}(\mathbf{K}) \end{bmatrix}, \quad \mathbf{C}^{(\alpha,j)}_{p}(\mathbf{K}) = \begin{bmatrix} \sum_{\eta=1}^{8N_{O,atom}} a_{p;\eta,0} b^{(\alpha,j)}_{\eta}(\mathbf{K}+\mathbf{G}_0) \\ \sum_{\eta=1}^{8N_{O,atom}} a_{p;\eta,1} b^{(\alpha,j)}_{\eta}(\mathbf{K}+\mathbf{G}_1) \end{bmatrix} \tag{21}$$

and the unitary matrix $\underline{\mathbf{U}}$ is

$$\underline{\mathbf{U}} = \frac{1}{\sqrt{2}} \begin{bmatrix} e^{i\boldsymbol{\rho}_0\cdot\mathbf{G}_0} & e^{i\boldsymbol{\rho}_0\cdot\mathbf{G}_1} \\ e^{i\boldsymbol{\rho}_1\cdot\mathbf{G}_0} & e^{i\boldsymbol{\rho}_1\cdot\mathbf{G}_1} \end{bmatrix} = \frac{1}{\sqrt{2}} \begin{bmatrix} 1 & 1 \\ 1 & -1 \end{bmatrix}. \tag{22}$$

As in Refs. 3 and 5, Eq. (22) is solved repeatedly for each atom-orbital pair (α,j), $\alpha=1,\ldots,N_{O,atom}$, $j=0,\ldots,7$, and the results are saved. Taking advantage of the normalization of the Bloch states yields the following relation:

$$\mathcal{P}_{p;n} = \sum_{\eta=1}^{8N_{O,atom}} |a_{p;\eta,n}|^2 = \sum_{\alpha}^{N_{O,atom}} \sum_{j=0}^{7} |[\mathbf{C}^{(\alpha,j)}_{p}]_n|^2,$$

$$[\mathbf{C}^{(\alpha,j)}_{p}]_n = \sum_{\eta=1}^{8N_{O,atom}} a_{p;\eta,n} b^{(\alpha,j)}_{\eta}(\mathbf{K}+\mathbf{G}_n), \tag{23}$$

where $\mathcal{P}_{p;n}$ represents the probability that the supercell state p projects onto the primitive-cell states of wave vector $\mathbf{k}=\mathbf{K}+\mathbf{G}_n$, $n=0,1$.

The probabilities $\mathcal{P}_{p;n}$ are computed and saved for all supercell states p and all primitive-cell states of wave vector $\mathbf{k}=\mathbf{K}+\mathbf{G}_n$, $n=0,1$. The resulting (energy) spectrum at fixed wave vector $\mathbf{k}=\mathbf{K}+\mathbf{G}_n$, $n=0,1$, is used in band determination. For a perfect structure such as the superlattice unfolded here, when primitive-cell bands for a given $\mathbf{k}$ are not degenerate (or nearly degenerate), each $\mathcal{P}_{p;n}$ projects onto a single primitive-cell state.[3] For alloys or other imperfect structures, at a fixed $\mathbf{k}$, the $\mathcal{P}_{p;n}$ typically forms peaks around energies which represent the approximate primitive-cell bands, and the resulting steplike cumulative probability function can be used in approximate band definition.[5]

III. RESULTS

The SiGe SL is modeled using the $sp^3d^5s^*$ empirical tight-binding approach.[8] The Si and Ge bulk parameters are taken from our earlier work.[9] The two-center integrals for a Si-Ge nearest-neighbor pair have been optimized using our genetic algorithm[10] to give the best $Si_{0.5}Ge_{0.5}$ bulk behavior within the virtual crystal approximation and are shown in Table I. Strain is present in the SL and alters both the two-center integrals and the on-site parameters. The two-center integrals are scaled using the customary generalization of Harrison's[11] d^{-2} scaling law: $U=U_0(d_0/d)^\eta$, where U_0 is an ideal two-center integral and d_0 and d are the ideal and actual bond lengths, respectively. The on-site parameter shifts are determined using our method presented in Ref. 12. The scaling exponents and shift constants are given in Tables II and III.

The behavior of the bulk Si and Ge band edges under biaxial and hydrostatic strain is shown in Figs. 4–7. For the

TABLE I. Nearest-neighbor two-center integrals for Si-Ge bonds (in eV).

Two-center integral	Value (eV)
$ss\sigma$	−1.574309
$s^*s^*\sigma$	−3.999753
$s(\mathrm{Si})s^*(\mathrm{Ge})\sigma$	−1.440045
$s(\mathrm{Ge})s^*(\mathrm{Si})\sigma$	−1.499091
$s(\mathrm{Ge})p(\mathrm{Si})\sigma$	2.760826
$s(\mathrm{Si})p(\mathrm{Ge})\sigma$	2.878285
$s^*(\mathrm{Ge})p(\mathrm{Si})\sigma$	2.814474
$s^*(\mathrm{Si})p(\mathrm{Ge})\sigma$	2.747303
$s(\mathrm{Ge})d(\mathrm{Si})\sigma$	−2.595310
$s(\mathrm{Si})d(\mathrm{Ge})\sigma$	−2.471630
$s^*(\mathrm{Ge})d(\mathrm{Si})\sigma$	−1.029594
$s^*(\mathrm{Si})d(\mathrm{Ge})\sigma$	−1.045346
$pp\sigma$	4.201374
$pp\pi$	−1.626914
$p(\mathrm{Ge})d(\mathrm{Si})\sigma$	−2.022367
$p(\mathrm{Si})d(\mathrm{Ge})\sigma$	−-1.415419
$p(\mathrm{Ge})d(\mathrm{Si})\pi$	2.504041
$p(\mathrm{Si})d(\mathrm{Ge})\pi$	2.023372
$dd\sigma$	−1.317709
$dd\pi$	2.501057
$dd\delta$	−-1.777856

TABLE II. Scaling exponents η (dimensionless) and unstrained lattice constants a_0 (nm) for two-center integrals between Si-Si, Ge-Ge, and Si-Ge.

	Si	Ge	Si-Ge
		η	
$ss\sigma$	0.56247	1.99551	2.155355
$s^*s^*\sigma$	0.19237	2.38823	0.00000
$ss^*\sigma$	0.13203	0.00000	0.154363
$sp\sigma$	2.36548	1.29303	2.157637
$s^*p\sigma$	0.34492	5.00000	1.413615
$sd\sigma$	2.56720	2.79244	1.831938
$s^*d\sigma$	1.08601	0.75134	2.538574
$pp\sigma$	0.49435	1.13641	2.621803
$pp\pi$	1.84385	1.74803	1.491652
$pd\sigma$	2.23636	2.68784	1.787961
$pd\pi$	4.51250	4.36921	2.257439
$dd\sigma$	4.66836	5.00000	1.814857
$dd\pi$	2.30238	0.69769	1.973166
$dd\delta$	0.92391	3.06253	1.805441
		a_0	
	0.543095	0.565790	0.554443

TABLE III. On-site parameter shift constants (dimensionless) and downward atomic shifts, E_{shift} (in eV, same for both atoms) for orbital pairs Si-Si, Ge-Ge, and Si-Ge.

	Si	Ge		Si-Ge
	C			C
ss	1.68054	0.00000	ss	3.09934
s^*s^*	0.77849	6.28624	s^*s^*	2.09695
ss^*	1.78613	1.86887	$s(\mathrm{Si})s^*(\mathrm{Ge})$	1.69301
			$s(\mathrm{Ge})s^*(\mathrm{Si})$	3.16404
sp	0.48057	2.03278	$s(\mathrm{Ge})p(\mathrm{Si})$	2.25252
			$s(\mathrm{Si})p(\mathrm{Ge})$	2.21094
s^*p	3.59244	6.28624	$s^*(\mathrm{Ge})p(\mathrm{Si})$	2.39048
			$s^*(\mathrm{Si})p(\mathrm{Ge})$	2.58548
sd	0.00000	0.16396	$s(\mathrm{Ge})d(\mathrm{Si})$	1.26252
			$s(\mathrm{Si})d(\mathrm{Ge})$	1.88788
s^*d	0.34243	1.98112	$s^*(\mathrm{Ge})d(\mathrm{Si})$	1.77635
			$s^*(\mathrm{Si})d(\mathrm{Ge})$	1.82653
pp	4.07053	0.42830	pp	2.89710
pd	0.00000	0.12084	$p(\mathrm{Ge})d(\mathrm{Si})$	1.26053
			$p(\mathrm{Si})d(\mathrm{Ge})$	3.51673
dd	5.30270	3.85908	dd	3.55811
	E_{shift}			E_{shift}
	27.0	27.77		27.0

biaxial strain and SL calculations, the z-lattice constant was determined using the Keating[13] model, with $(\alpha_{\mathrm{Si}},\beta_{\mathrm{Si}})=(48.5,13.8)$, $(\alpha_{\mathrm{Ge}},\beta_{\mathrm{Ge}})=(39.0,12.0)$ N/m; for the SL, $a_{\parallel}=a_{\mathrm{Si}}$. The valence band maxima of both materials and the X-valley conduction-band minima of Si and the L-valley minima of Ge were optimized to reproduce the predictions of van de Walle's model solid theory.[14] The split-off holes were

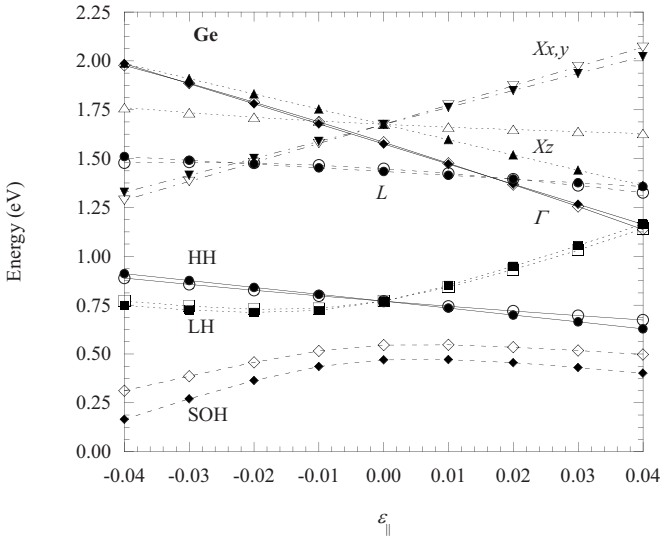

FIG. 4. Biaxial strain behavior of Ge using our parameter set (open symbols) and the model solid theory of Ref. 14 (solid symbols). X denotes X-valley minima, which generally occur a little away from the symmetry point.

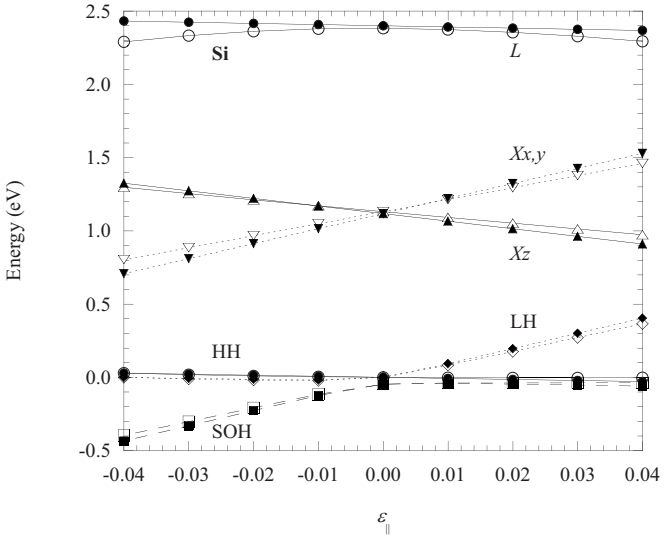

FIG. 5. Biaxial strain behavior of Si using our parameter set (open symbols) and the model solid theory of Ref. 14 (solid symbols). X denotes X-valley minima, which generally occur a little away from the symmetry point.

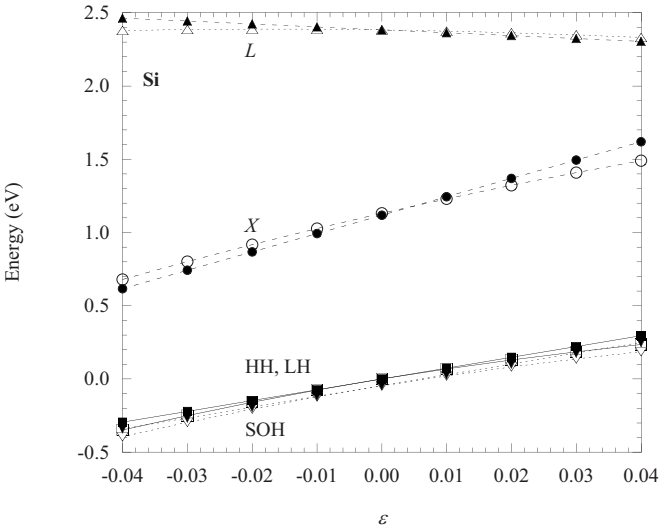

FIG. 7. Hydrostatic strain behavior of Si using our parameter set (open symbols) and the model solid theory of Ref. 14 (solid symbols). X denotes X-valley minima, which generally occur a little away from the symmetry point.

not strongly weighted in the optimization, however. The unoptimized biaxial strain behaviors of the Ge-X_z minima and the Si-L minima differ from van de Walle's predictions[14] and are, in fact, closer to the behavior predicted by the pseudopotential calculations of Fischetti and Laux.[15] For both hydrostatic and biaxial strains, there is a fairly wide variation in the calculated behavior in the literature (see Refs. 14–17).

Figure 8 shows our calculation of the bands along [100] for the Si(4)Ge(4) SL discussed above. The bands were unfolded using the method of Sec. II from calculations based on the rectangular cell of Fig. 2, which has two nonidentical primitive cells. The Lanczos method[18] was used to calculate the eigenvectors, and an especially stringent minimum band probability[5] of 90% was used in the zone-unfolding calculation, except at the highly degenerate folding point corresponding to $\mathbf{k}=(\pi/a_{\parallel})\mathbf{e}_x$. (At points of high degeneracy, often only one of a pair of degenerate eigenvectors is returned by the Lanczos method,[18] so a lower criterion of 50% was used.) Note that the resolution is very good. Our calculations give a minimum (indirect) gap of 0.825 eV and a minimum direct gap of 1.048 eV; the next-higher direct gaps are 1.099, 1.728, and 1.743 eV. The experiments of Pearsall *et al.*[6] measured a minimum gap (direct) of 0.76 eV, with next-higher gaps of 1.25, 2.31, and 2.58 eV. The LMTO calculations by Ikeda *et al.*[7] found a minimum direct gap of about 1.27 eV, with next-higher direct gaps of 1.28, 1.66, and

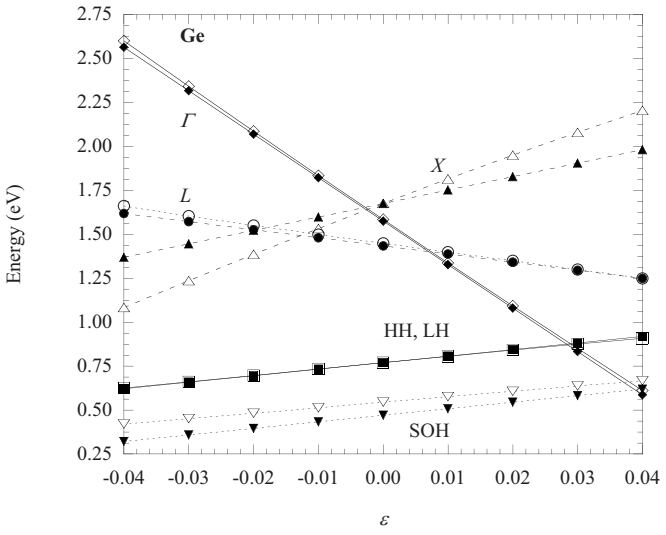

FIG. 6. Hydrostatic strain behavior of Ge using our parameter set (open symbols) and the model solid theory of Ref. 14 (solid symbols). X denotes X-valley minima, which generally occur a little away from the symmetry point.

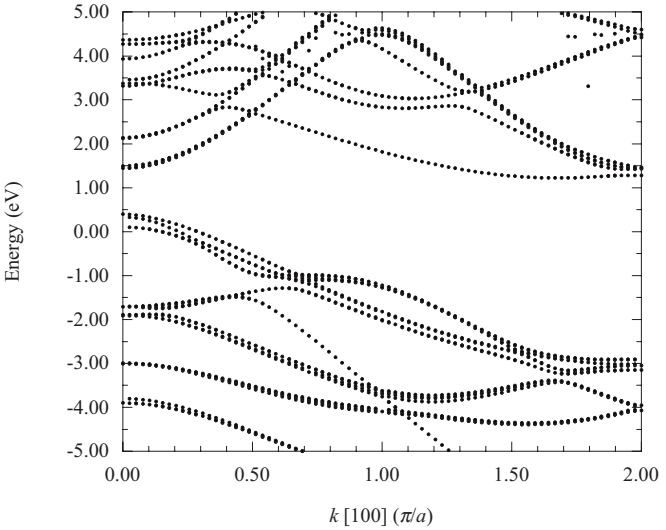

FIG. 8. Unfolded bands along [100] for the Si(4)Ge(4) SL. The bands were unfolded using the method presented here from calculations employing the rectangular cell of Fig. 2, which has two nonidentical primitive cells.

1.68 eV in their ideal interface model, for their diffuse interface model, the minimum direct gap is about 1.04 eV. Although our lowest direct gap is smaller than that of Ikeda *et al.*,[7] it does not by itself account for the observed 0.76 eV transition, whose exact nature remains unresolved.

IV. CONCLUSIONS

We have shown that zone unfolding is possible even when the nonprimitive unit cell contains primitive cells which are not equivalent. We have shown how the allowed wave vectors must be chosen and have modified our zone-unfolding method[5] to implement this process. We have used this modified method to unfold the bands of a Si(4)Ge(4) SL studied both experimentally[6] and theoretically[7] and have achieved results in general agreement with earlier work. In addition, we give strain parameters for bulk Si and Ge and both two-center integrals and strain parameters for Si-Ge nearest-neighbor pairs in the $sp^3d^5s^*$ empirical tight-binding approach.[8] Because our modified method gives primitive-cell dispersion relations from nonprimitive rectangular cells with nonequivalent primitive cells, general nanodevice simulation tools become simpler to construct. A set, easily programed rectangular cell can be used, and the method presented here can still unfold the true primitive-cell $E(\mathbf{k})$ relations.

ACKNOWLEDGMENTS

This work was supported by Semiconductor Research Corporation. We thank E. Ingram for expert help with the figures.

[1] G. Klimeck, F. Oyafuso, T. B. Boykin, R. C. Bowen, and P. von Allmen, Comput. Model. Eng. Sci. **3**, 601 (2002).
[2] NEMO3D development is being continued by the Network for Computational Nanotechnology (NCN). Simulations were performed on nanoHUB. org resources. nanoHUB. org is a web site dedicated to advancing nanotechnology through theory, modeling, and simulation for research and education.
[3] T. B. Boykin and G. Klimeck, Phys. Rev. B **71**, 115215 (2005).
[4] T. B. Boykin, N. Kharche, and G. Klimeck, Eur. J. Phys. **27**, 5 (2006).
[5] T. B. Boykin, N. Kharche, G. Klimeck, and M. Korkusinski, J. Phys.: Condens. Matter **19**, 036203 (2007).
[6] T. P. Pearsall, J. Bevk, L. C. Feldman, J. M. Bonar, J. P. Mannaerts, and A. Ourmazd, J. Vac. Sci. Technol. B **5**, 1274 (1987); Phys. Rev. Lett. **58**, 729 (1987); **58**, 1053 (1987).
[7] M. Ikeda, K. Terakura, and T. Oguchi, Phys. Rev. B **48**, 1571 (1993).
[8] J. M. Jancu, R. Scholz, F. Beltram, and F. Bassani, Phys. Rev. B **57**, 6493 (1998).
[9] T. B. Boykin, G. Klimeck, and F. Oyafuso, Phys. Rev. B **69**, 115201 (2004).
[10] G. Klimeck, R. C. Bowen, T. B. Boykin, C. Salazar-Lozaro, T. A. Cwik, and A. Stoica, Superlattices Microstruct. **27**, 77 (2000); G. Klimeck, R. C. Bowen, T. B. Boykin, and T. A. Cwik, *ibid.* **27**, 519 (2000).
[11] J. M. Wills and W. A. Harrison, Phys. Rev. B **28**, 4363 (1983).
[12] T. B. Boykin, G. Klimeck, R. C. Bowen, and F. Oyafuso, Phys. Rev. B **66**, 125207 (2002).
[13] P. N. Keating, Phys. Rev. **145**, 637 (1966).
[14] C. G.Van de Walle, Phys. Rev. B **39**, 1871 (1989).
[15] M. V. Fischetti and S. E. Laux, J. Appl. Phys. **80**, 2234 (1996).
[16] M. M. Rieger and P. Vogl, Phys. Rev. B **48**, 14276 (1993).
[17] S.-H. Wei and A. Zunger, Phys. Rev. B **60**, 5404 (1999).
[18] G. H. Golub and C. F. van Loan, *Matrix Computations* (Johns Hopkins University Press, Baltimore, 1989), Chap. 9